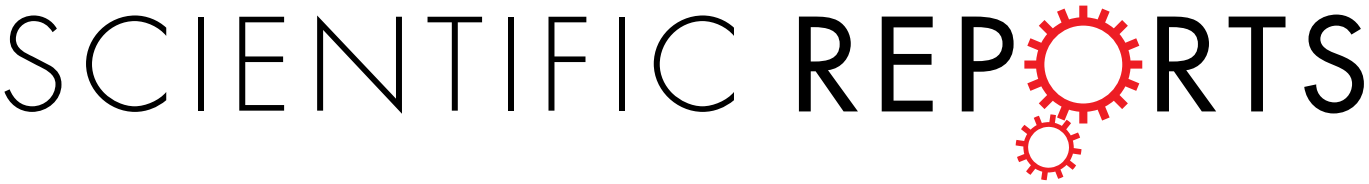

OPEN

Broadband multiple responses of surface modes in quasicrystalline plasmonic structure

Received: 23 March 2016
Accepted: 11 July 2016
Published: 05 August 2016

Haiming Yuan[1,2], Xiangqian Jiang[1,2], Feng Huang[1,2] & Xiudong Sun[1,2]

We numerically study the multiple excitation of surface modes in 2D photonic quasicrystal/metal/substrate structure. An improved rigorous coupled wave analysis method that can handle the quasicrystalline structure is presented. The quasicrystalline lattice, which refers to Penrose tiling in this paper, is generated by the cut-and-project method. The normal incidence spectrum presents a broadband multiple responses property. We find that the phase matching condition determines the excitation frequency for a given incident angle, while the depth of the reflection valley depends on the incident polarization. The modes will split into several sub-modes at oblique incidence, which give rise to the appearance of more responses on the spectrum.

Broadband multiple responses is one of the keys to realize high efficient solar cell[1,2], broadband absorber[3,4], and so on[5,6]. There are many ways to broaden the region of interaction frequency, such as using trapezoid units[7], fractal structure[8] and photonic quasicrystal[2,3]. Photonic quasicrystal (QC) is a class of structures lacking of traditional symmetry, in which blocks are arranged only with long-range order[5,9]. The Fourier transformation of the photonic QC gives a set of reciprocal vectors with multi-fold symmetric, which makes the phase matching condition satisfied at various incident frequencies. Correspondingly, these modes could be excited simultaneously under a broadband source, which could be used for increasing the efficiency of energy harvest in solar cell system[1,2,10,11]. The optical response could also be optimized by engineering the density of the spatial frequencies[12]. Plasmonic quasicrystals attract much attention for its various penitential applications[13]. Zi-Lan Deng *et al.* investigate the plasmonic modes in a two dimensional quasicrystalline array of metal nanoparticles with the eigen-decomposition method and two anti-phase ring modes with different polarizations are found to be of high fidelity and high spatial localization[14]. Nanoparticles arranged in both 1D and 2D Fibonacci pattern are also demonstrated to be used in controlling and optimizing the local field enhancement and localization[15], the in-plane optical mode symmetry[16], and so on[17].

In evaluating electromagnetic response of photonic QC, the lacking of short-range order makes periodic boundary conditions no longer be applicable. We must simulate a large enough structure to obtain the long range order property, which makes the traditional numerical methods, including finite-difference time-domain and finite element method, computationally expensive, especially for the 2D photonic QC. Supercell approach is also unable to improve the computational efficiency radically[18,19]. In the simulation model of ref. 1, several parameters need to be fitted from the normal incidence spectra of a periodic gold disk arrangement by using the scattering matrix calculations.

As a semi-analysis method, the traditional rigorous coupled wave analysis (RCWA) has advantages in dealing with the photonic crystals, such as 1D grating, 2D square lattice, and even the hexagonal lattice[20]. However, the traditional RCWA needs to be improved to handle the irregular lattice as quasicrystalline structures. In mathematics, quasicrystalline lattice can be obtained by using the cut-and-project method from a higher dimensional space. For example, 1D Fibonacci sequence is generated from the 2D grid to a 1D line and the 2D Penrose tiling is generated from the 5D grid to a 2D plane. It is found that the cut-and-project process does not lose the periodicity of the higher dimensional space. Therefore, the intrinsic periodicity in the quasicrystalline lattice makes the Floquet's theory still be effective and the RCWA has been used to calculate the 1D Fibonacci grating[19]. Utilization the RCWA on studying the diffraction properties of 2D octagonal quasicrystalline structure is also found[21,22].

In this paper, we study the surface modes excitation in the photonic QC/metal film structure. First, the algorithm of the improved RCWA which can handle the quasicrystalline structures is derived. We choose the

[1]Department of Physics, Harbin Institute of Technology, Harbin 150001, China. [2]Key Lab of Micro-Optics and Photonic Technology of Heilongjiang Province, Harbin 150001, China. Correspondence and requests for materials should be addressed to X.S. (email: xdsun@hit.edu.cn)

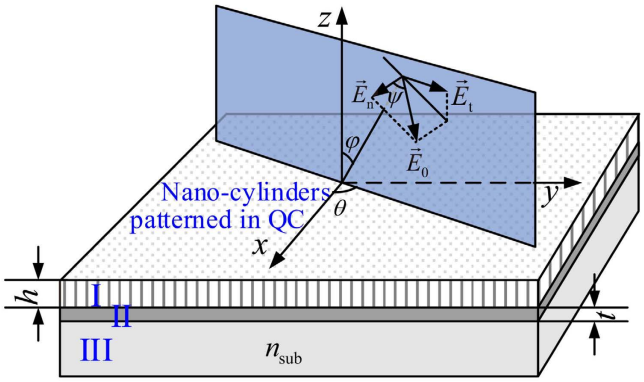

Figure 1. The geometry of the photonic QC/metal film structures and the coordinate configuration. I, II and III are the photonic QC with the cross section as Fig. 2(a), the metal layer and the substrate, respectively. (θ, φ) represents the incident direction and ψ represents the polarization. In this paper, the spectra is calculated with $\theta = \psi = \pi/2$.

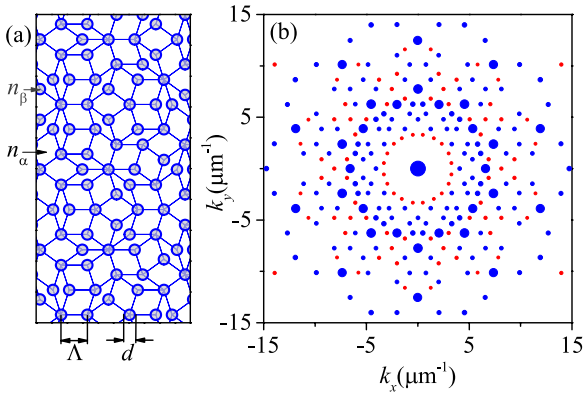

Figure 2. (**a**) The cross section of the photonic QC layer. The gray nano-cylinders of refractive index n_β are patterned in the quasicrystalline lattice with background index n_α. (**b**) The Fourier transformation of the quasicrystalline cross section of (**a**) for $\Lambda = 1\,\mu m$ and $d = 0.4\Lambda$. The area of each circle is proportional to the spacial spectrum intensity. The circles marked blue are the first 231 reciprocal vectors chosen to be the base vectors.

quasicrystalline lattice to be the Penrose tiling. Then, we numerically simulate the multiple modes excitation process by the improved new RCWA program. Each of the modes could be identified by comparing with the mode analysis results under the effective media theory. Phase matching condition is still effective, and the excitation intensity is related to the incident polarization. Multiple splitting behavior at the oblique incidence is also found on the spectrum. Modes interactions are also presented by changing the QC constant.

Method

The proposed photonic QC/metal layer structure on a substrate is as sketched in Figs 1 and 2(a). The quasicrystalline lattice of Penrose tiling is generated by the cut-and-project method from 5D grid to 2D plane[5,23–25]. The dielectric nano-cylinders of refractive index n_α are patterned in the quasicrystalline lattice with background index n_β. d is the diameter of the nano-cylinders and the QC constant Λ is side length of the cells of the Penrose tiling as shown in Fig. 2(a). The thickness of photonic QC and metal film are h and t, respectively. The structure is placed on the substrate with refractive index of n_{sub}. (θ, φ) and ψ are used to describe incident angle and incident polarization, respectively.

The RCWA is a semi-analytical method base on the Floquet's theory. By Fourier transformation, continuous Maxwell equations can be discretized into matrix equations. Then, the eigenmodes can be numerically obtained by solving the eigenvalues and the eigenvectors of the matrix equations. The field in the structure is a linear combination of the eigenmodes. At last, the reflectivity, transmissivity and the field distributions can be obtained by solving the matrix equations establish through the boundary conditions. Two main differences between the traditional RCWA and the improved algorithm in this paper are the choice of the reciprocal vectors and the assembly of the material matrix, which embodies the coupling process between the constituent waves(or Fourier components). The key of the algorithm is to establish a matrix by analyzing the relationship among the reciprocal vectors of the 2D quasicrystalline lattice.

The first step is to discretize Maxwell equations. Without lost of generality, Q nano-cylinders distribute in a big circle with radius R_0. The permittivity distribution of the cross section as shown in Fig. 2(a) can be expressed in the convolution form as

$$\varepsilon(\vec{r}) = \varepsilon_\alpha + (\varepsilon_\beta - \varepsilon_\alpha)\mathrm{circ}(|\vec{r}|/r_0) * \sum_{q=1}^{Q}\delta(\vec{r} - \vec{r}_q), \tag{1}$$

where $\vec{r}_n$ is the center of the *nth* nano-cylinder, "*" represents convolution, $\varepsilon_\alpha = n_\alpha^2, \varepsilon_\beta = n_\beta^2, \vec{r} = (x, y)$ and r_0 is the radius of the nano-cylinder. For the diffraction pattern of any lattice (periodic, aperiodic or quasiperiodic) being a discrete set of points, the Fourier transformation of quasicrystalline lattice should also be a set of Dirac delta functions[5,23]. It is possible of expending equation (1) in the form of

$$\varepsilon(\vec{r}) = \sum_{m=1}^{M}\varepsilon_m(\vec{k}_m)e^{i\vec{k}_m\cdot\vec{r}}, \tag{2}$$

where the base vectors $\vec{k}_m = (k_{x,m}, k_{y,m})$ are the discrete reciprocal vectors of quasicrystalline lattice in the reciprocal space. The expansion coefficients ε_m can be easily derived as

$$\varepsilon_m(\vec{k}_m) = \varepsilon_\alpha\delta(\vec{k}_m, 0) + (\varepsilon_\beta - \varepsilon_\alpha)\frac{r_0 J_1(r_0|\vec{k}_m|)}{|\vec{k}_m|}\frac{2}{R_0^2}\sum_{q=1}^{Q}e^{-i\vec{k}_m\cdot\vec{r}_q}, \tag{3}$$

where J_1 is the Bessel function of the first kind. In calculation, we generate $Q\sim1.3$ million quasiperiodic points by the cut-and-project method. The result of $\varepsilon_m(\vec{k}_m)$ is calculated with $d = 2r_0 = 0.4\Lambda = 0.4\,\mu\mathrm{m}$ and has shown in Fig. 2(b). Larger R_0 with large Q means the more accurate of the Fourier transformation and $R_0 = 500$ with $Q\sim1.3$ million are enough in the calculation. As expected, the nonzero $\varepsilon_m(\vec{k}_m)$ only appear at the terminal points of the base vectors, which are marked in circles. The area of each circle is proportional to the spacial frequency spectrum intensity $|\varepsilon_m(\vec{k}_m)|$.

The fields are expanded into the summary of each constituent waves:

$$\begin{aligned}\vec{E}(\vec{r}, z, t) &= \sum_{m=1}^{M}\left[E_{x,m}(z), E_{y,m}(z), E_{z,m}(z)\right]e^{i(\vec{k}_m\cdot\vec{r}-\omega t)}\\ \vec{H}(\vec{r}, z, t) &= \sum_{m=1}^{M}\left[H_{x,m}(z), H_{y,m}(z), H_{z,m}(z)\right]e^{i(\vec{k}_m\cdot\vec{r}-\omega t)},\end{aligned} \tag{4}$$

Substitute equation (2) and equation (4) into Maxwell equations, we obtain the matrix equations:

$$\begin{aligned}\partial_z\mathbf{H}_y &= i\mathbf{K}_y\mathbf{H}_z + i\omega\varepsilon_0\mathbf{M}_\varepsilon\mathbf{E}_x\\ \partial_z\mathbf{H}_x &= i\mathbf{K}_x\mathbf{H}_z - i\omega\varepsilon_0\mathbf{M}_\varepsilon\mathbf{E}_y\\ \partial_z\mathbf{E}_y &= i\mathbf{K}_y\mathbf{E}_z - i\omega\mu_0\mathbf{H}_x\\ \partial_z\mathbf{E}_x &= i\mathbf{K}_x\mathbf{E}_z + i\omega\mu_0\mathbf{H}_y\\ \mathbf{E}_z &= \mathbf{M}_\varepsilon^{-1}(-\mathbf{K}_x\mathbf{H}_y + \mathbf{K}_y\mathbf{H}_x)/\omega\varepsilon_0\\ \mathbf{H}_z &= (\mathbf{K}_x\mathbf{E}_y - \mathbf{K}_y\mathbf{E}_x)/\omega\mu_0\end{aligned}, \tag{5}$$

where $\mathbf{E}_x$, $\mathbf{E}_y$, $\mathbf{E}_z$, $\mathbf{H}_x$, $\mathbf{H}_y$ and $\mathbf{H}_z$ are column vectors constructed with elements of $E_{x,m}$, $E_{y,m}$, $E_{z,m}$, $H_{x,m}$, $H_{y,m}$ and $H_{z,m}$, respectively, and $\mathbf{K}_x$ and $\mathbf{K}_y$ are diagonal matrixes constructed with elements of $k_{x,m}\delta_{m,n}$ and $k_{y,m}\delta_{m,n}$, respectively. $\delta_{m,n}$ is the Kronecker delta. For arbitrary m and n, one will always find a $\vec{k}_p$ in the ordered set of base vectors satisfying

$$\vec{k}_p = \vec{k}_m - \vec{k}_n, \tag{6}$$

and the element of the material matrix in equation (5) is just $\mathbf{M}_{\varepsilon,m,n} = \varepsilon_{m,n} = \varepsilon_p(\vec{k}_p)$. In the traditional RCWA method, equation (6) is equivalent to $p = m - n$. However, for the quasicrystalline structure, the only way to confirm the order p is to traverse the ordered set of base vectors, searching for $\vec{k}_m - \vec{k}_n$.

The properties of the structures are embodied in the material matrix $\mathbf{M}_\varepsilon$. For homogeneous layers (the layers of air, metal and substrate), $\mathbf{M}_\varepsilon$ is simply a diagonal matrix. The constituent wave, corresponding to each term of equation (4), propagates independently without coupling. In the photonic QC layer, the nonzero element of $\mathbf{M}_{\varepsilon,m,n}$ denotes the coupling intensity between the constituent waves with $\vec{k}_m$ and $\vec{k}_n$.

Equation (5) is an eigenvalue problem essentially. By eliminating $\mathbf{E}_x$, $\mathbf{E}_y$, $\mathbf{E}_z$, $\mathbf{H}_x$, $\mathbf{H}_y$ and $\mathbf{H}_z$, equation (5) can be simplified to a matrix equation:

$$\mathbf{M}_E\begin{bmatrix}\mathbf{E}_x\\ \mathbf{E}_y\end{bmatrix} = \partial_z^2\begin{bmatrix}\mathbf{E}_x\\ \mathbf{E}_y\end{bmatrix} \tag{7}$$

where

$$\begin{aligned}
\mathbf{M}_{E,1,1} &= \left(\mathbf{K}_x\mathbf{M}_\varepsilon^{-1}\mathbf{K}_x\mathbf{M}_\varepsilon + \mathbf{K}_y\mathbf{K}_y - k_0^2\mathbf{M}_\varepsilon\right)\\
\mathbf{M}_{E,1,2} &= \left(\mathbf{K}_x\mathbf{M}_\varepsilon^{-1}\mathbf{K}_y\mathbf{M}_\varepsilon - \mathbf{K}_y\mathbf{K}_x\right)\\
\mathbf{M}_{E,2,1} &= \left(\mathbf{K}_y\mathbf{M}_\varepsilon^{-1}\mathbf{K}_x\mathbf{M}_\varepsilon - \mathbf{K}_x\mathbf{K}_y\right)\\
\mathbf{M}_{E,2,2} &= \left(\mathbf{K}_y\mathbf{M}_\varepsilon^{-1}\mathbf{K}_y\mathbf{M}_\varepsilon + \mathbf{K}_x\mathbf{K}_x - k_0^2\mathbf{M}_\varepsilon\right)
\end{aligned} \tag{8}$$

Matrix $\mathbf{M}_E$ is divided into four blocks and the two coordinates in the subscript of equation (8) label the position of each block. By solving the eigenvalue problem of equation (7), we obtained the eigenmodes as a combination of the constituent waves of $\exp(i\vec{k}_m \cdot \vec{r})$. The combination coefficients are just the eigenvector $\mathbf{W}_m$ (a column vector with 2M elements and $m = 1 \cdots 2M$) with the eigenvalue β_m^2 and β_m is the propagation constant of the eigenmodes. Meanwhile, the eigenvectors corresponding to the magnetic field can be obtained as well:

$$\mathbf{V} = \mathbf{M}_H\mathbf{W}\boldsymbol{\beta}^{-1}, \tag{9}$$

where $\boldsymbol{\beta}$ is a diagonal matrix with element $\beta_m\delta_{m,n}$, matrix $\mathbf{W}$ is constructed by $\mathbf{W}_m$ and

$$\begin{aligned}
\mathbf{M}_{H,1,1} &= -\mathbf{K}_x\mathbf{K}_y/\omega\mu_0\\
\mathbf{M}_{H,1,2} &= (\mathbf{K}_x\mathbf{K}_x - k_0^2\mathbf{M}_\varepsilon)/\omega\mu_0\\
\mathbf{M}_{H,2,1} &= (-\mathbf{K}_y\mathbf{K}_y + k_0^2\mathbf{M}_\varepsilon)/\omega\mu_0\\
\mathbf{M}_{H,2,2} &= \mathbf{K}_y\mathbf{K}_x/\omega\mu_0
\end{aligned} \tag{10}$$

Notice that $\mathbf{M}_H$, $\mathbf{W}$ and $\boldsymbol{\beta}$ are all 2M by 2M matrix. The field in layer n is the linear combination of the 2M eigenmodes. The combination coefficients express as column vectors $\mathbf{c}_n^{\pm}$ with 2M elements. "+" in the superscript represent the propagation direction of the eigenmode is along the incidence and and "−" corresponds to the opposite. $\mathbf{c}_n^{\pm}$ and $\mathbf{c}_{n+1}^{\pm}$ are related by the boundary conditions that the tangential component of $\mathbf{E}$ and $\mathbf{H}$ must be continuous at $n|n+1$ interface. For a N interfaces system, N matrix equations are established:

$$\begin{aligned}
&\mathbf{M}_{1,L}\begin{bmatrix}\mathbf{I}\\ \mathbf{R}\end{bmatrix} = \mathbf{M}_{2,R}\begin{bmatrix}\mathbf{c}_2^+\\ \mathbf{c}_2^-\end{bmatrix}\\
&\cdots\\
&\mathbf{M}_{n,L}\begin{bmatrix}\mathbf{c}_n^+\\ \mathbf{c}_n^-\end{bmatrix} = \mathbf{M}_{n+1,R}\begin{bmatrix}\mathbf{c}_{n+1}^+\\ \mathbf{c}_{n-1}^+\end{bmatrix}\\
&\cdots\\
&\mathbf{M}_{N,L}\begin{bmatrix}\mathbf{c}_N^+\\ \mathbf{c}_N^-\end{bmatrix} = \mathbf{M}_{N+1,R}\begin{bmatrix}\mathbf{T}\\ \mathbf{0}\end{bmatrix}
\end{aligned} \tag{11}$$

where

$$\mathbf{M}_{n,L} = \begin{bmatrix}\mathbf{W}_n\mathbf{X}_n & \mathbf{W}_n\\ \mathbf{V}_n\mathbf{X}_n & -\mathbf{V}_n\end{bmatrix}, \mathbf{M}_{n,R} = \begin{bmatrix}\mathbf{W}_n & \mathbf{W}_n\mathbf{X}_n\\ \mathbf{V}_n & -\mathbf{V}_n\mathbf{X}_n\end{bmatrix}. \tag{12}$$

and $\mathbf{I}$ represent the incident field with the nonzero elements $\mathbf{I}_{m_0} = E_{x,m_0}$ and $\mathbf{I}_{m_0+M} = E_{y,m_0}$ (m_0 is the zero-order diffraction, $\vec{k}_{m_0} = 0$). For the normal incidence of TM-polarization, we should set $E_{x,m_0} = 0$ and $E_{y,m_0} = E_0$. $\mathbf{X}_n$ is a diagonal matrix with element and $exp(i\beta_m t)$. The field in the structure can be rebuilt with $\mathbf{I}$, $\mathbf{R}$, $\mathbf{T}$ and $\mathbf{c}_n^{\pm}$, which are solved from equation (11). Taking the reflection field for example, we calculate $E_{m,x}^{\mathrm{R}}$ and $E_{m,y}^{\mathrm{R}}$ from

$$\begin{bmatrix}\mathbf{E}_{x,R}\\ \mathbf{E}_{y,R}\end{bmatrix} = \mathbf{W}_1\mathbf{R}. \tag{13}$$

and $E_{m,z}^{\mathrm{R}}$ can be calculated from equation (5). The intensity of m-order diffraction is

$$I_m^{\mathrm{R}} = \frac{1}{2}n_1 c\varepsilon_0 \sum_{i=x,y,z}\left|E_{m,i}^{\mathrm{R}}\right|^2, \tag{14}$$

where n_1 is the refractive index region 1. The incident intensity $I_{m_0}^{\mathrm{I}}$ and the transmissive intensity I_m^{T} can also be obtained similarly. And the reflectivity and the transmissivity are

$$R = \sum_{m=1}^{M}\frac{I_m^R}{I_0^I}\,\mathrm{Re}\left(\frac{k_{z,m}^R}{k_{z,m_0}^R}\right),\ T = \sum_{m=1}^{M}\frac{I_m^T}{I_0^I}\,\mathrm{Re}\left(\frac{k_{z,m}^T}{k_{z,m_0}^T}\right) \tag{15}$$

where $k_{m,z}^R = (n_1^2k_0^2 - k_{m,x}^2 - k_{m,x}^2)^{1/2}$ and $k_{m,z}^T = (n_{N+1}^2k_0^2 - k_{m,x}^2 - k_{m,x}^2)^{1/2}$. If the plane wave incident at the direction of (θ, φ) with polarization of ψ, two extra steps should be added into the algorithm:

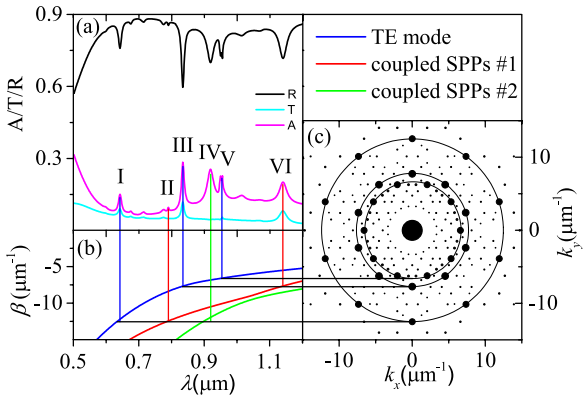

Figure 3. (**a**) The reflection/transmission/absorption spectrum of normal incidence. (**b**) The dispersion relations from the mode analysis of the air/effective media/metal film/substrate structure. The blue line is TE mode. The red and the green line are the coupled SPPs along the upper/lower metal surface. (**c**) The reciprocal vectors in reciprocal space.

$$\begin{aligned} E_{x,m_0} &= E_0 \cos\psi \\ E_{y,m_0} &= E_0 \sin\psi \cos\varphi \\ \mathbf{K}_x &\rightarrow \mathbf{K}_x \cos\theta' - \mathbf{K}_y \cos\theta' \\ \mathbf{K}_y &\rightarrow \mathbf{K}_x \sin\theta' + \mathbf{K}_y \cos\theta' - n_1 k_0 \sin\varphi \end{aligned} \tag{16}$$

where $\theta' = \theta - \pi/2$. To improve the numerical stability, we make the same transformation as ref. 26 did, trying to avoid calculating the inverse matrix. For the metallic quasicrystalline structure, although the base mode up to $M = 421$, it is found that the improved RCWA couldn't be convergent. In the derivation, neither the quasicrystalline lattice is confined to the Penrose tiling, nor the unit is confined to the cylinder. Hence, the algorithm can be directly applied to other quasicrystalline structure with only the modification on equation (3).

Results

The parameters used in the calculation are $n_\alpha = 2.4$, $n_\beta = 2.0$, $h = 0.1\,\mu$m, $t = 0.05\,\mu$m, and $n_{sub} = 1.5$. The permittivity of silver comes from the Brendel-Bormann model[27]. As is discussed previously, $|\varepsilon_{m,n}|$ denotes the coupling intensity between constituent waves with wave vector $\vec{k}_m$ and $\vec{k}_n$. Small $|\varepsilon_{m,n}|$ means weak energy flow between these two constituent waves. In other words, when $|\varepsilon_m(\vec{k}_m)|$ is small enough, the base vector $\vec{k}_m$ could be ignored with acceptable accuracy. We sort $\vec{k}_m$ by $|\varepsilon_m(\vec{k}_m)|$ in descending order and take the first M of $\vec{k}_m$'s as the base vectors. It is found that when the cut-off percentage brings down to 5% (i.e., $5\%|\varepsilon_m(\vec{k}_m)|$), the reflective spectrum becomes stable. It means that we can choose the first 231 of $\vec{k}_m$'s, which are marked blue in Fig. 2(b), as the base vectors in calculating the spectrum.

Figure 3(a) shows the reflection/transmission/absorption spectrum for TM-polarized normal incidence. The complex spectrum structure means that a serious of surface waves are excited in the region of $\lambda \in (0.5\,\mu\text{m}, 1.2\,\mu\text{m})$.

To identify these reflection valleys on the spectrum, we analyze both the TE and TM modes in the multilayer structure. Under the effective medium theory, the photonic QC is simplified to a homogeneous layer with effective index $n_{\text{eff}} = (1-f)n_\alpha + fn_\beta \approx 2.06$, where $f \equiv S_\alpha/(S_\alpha + S_\beta)$, S_α represent the sum of the areas of the nano-cylinders and S_β represent the area of the rest. The dispersion relations, including a TE waveguide (blue) and two surface plasmon polaritons(SPPs, red and green), are plotted in Fig. 3(b). The repulsion of two SPPs branches (red and green) means that strong coupling exists between the SPPs on the upper and lower interface.

In the excitation process of 2D modes, the phase matching condition reads

$$\vec{\beta}(\lambda) = \vec{k}_t + \vec{k}_m, \tag{17}$$

where $\vec{\beta}$ is the wave vector of the excitation mode, $\vec{k}_t$ is the tangential component of incident wave vector projecting to the xy plane and $\vec{k}_m$ is the reciprocal vector of QC. Because of the internal 10-fold symmetry, when $\vec{k}_t = 0$ at normal incidence, each of ten reciprocal vectors on the same circle should satisfy equation (17) simultaneously. It means that each reflection valley in Fig. 3(a) corresponds to the ten surface waves with same $|\vec{\beta}(\lambda)| = |\vec{k}_m|$ but different propagation directions. These degenerate modes will be separates at oblique incidence. The connection between Fig. 3(a,b,c) are established by the vertical and horizon color lines. Mode I, III and V correspond to the same dispersion relation of blue curve in Fig. 3(b) but three different circles with three radiuses of $|\vec{k}_m|$ in Fig. 3(c). Because the dispersion relation of blue curve refers to the TE mode, these three modes are determined to be the TE modes guided by the photonic QC layer. Mode II, IV and VI correspond to the dispersion relations of red and green curves in Fig. 3(b). Because the dispersion relations of red and green curves refer to SPPs, these three modes are determined to be the SPPs on the upper and lower metal surface.

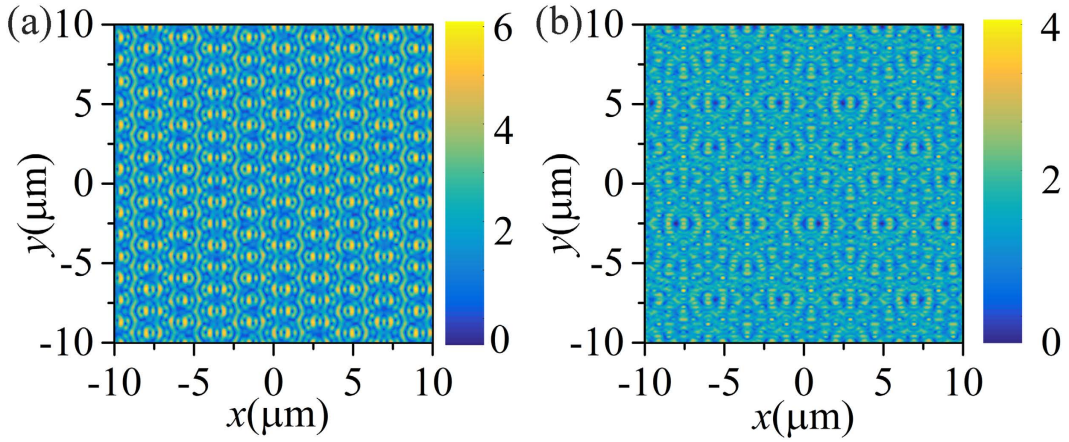

Figure 4. The field distributions of $|E|$ at upper surface of metal film for normal incidence. (**a**,**b**) correspond to mode III at $\lambda = 0.833\,\mu m$ and mode IV at $\lambda = 0.922\,\mu m$, respectively. (see Fig. 3).

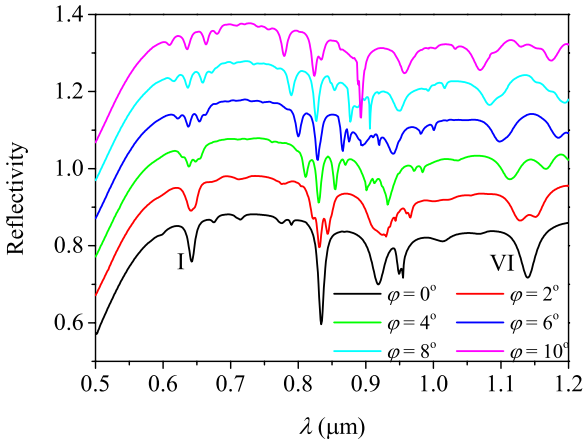

Figure 5. The reflection spectra with incident angle $\varphi = 0° \sim 10°$ ($\psi = \theta = \pi/2$). The vertical axis corresponds to the black solid line. Others shift up 0.1 by tune.

Taking mode III at $\lambda = 0.833\,\mu m$ and mode IV at $\lambda = 0.922\,\mu m$ as examples, we plot the field distribution of $|E|$ at upper surface of metal film in Fig. 4(a,b), respectively. The field distributions for normal incidence just behave as the standing wave with nodes, which means the surface waves at opposite directions are excited at the same time. It is also found that the main propagation directions of mode III and IV are different, which result from the polarization differences between TE mode and SPPs. It will be discussed in detail in the later sections.

For oblique incidence of $\varphi \neq 0$, the spectrum shows a complex splitting behavior as plotted in Fig. 5. When $\varphi \neq 00$, although the $\vec{k}_m$'s on the same circle are equal in magnitude, the nonzero $\overline{k}_t$ makes $|\vec{k}_t + \overline{k}_m|$'s no longer degenerate. For the $\overline{k}_m$'s on the small circle in Fig. 3(c), six sub-reflection-valleys should appear in theory, and for the $\overline{k}_m$'s on the middle and large circles, five sub-reflection-valleys should appear. Yet, not all of these sub-modes are found in Fig. 5. It is difficult to analyze mode II ~ V for the complex superposition. Therefore, we concentrate on mode I and VI. They obviously don't split into five sub-modes as the analysis. Especially for mode VI, the reflection valley performs like a double split behaviour. We attribute the sub-mode absence to the polarization.

Firstly, let's focus on mode I. As a TE-polarized mode, the magnetic field is on the plane determined by z axis and $\overline{\beta}_I$, and the electric field is perpendicular to this plane. On the other hand, as TM-polarized incidence, the electric field is on yz plane and the magnetic field is along x axis. We infer that the excitation intensity is determined by the angle between incident field and mode field. The sub-mode with $\overline{\beta}_I$ along x axis has electric field along y axis, just matching the electric field of incidence. It means that the sub-modes with $\overline{\beta}_I$ close to the x axis should be strongly excited. The depth of the reflection valley is proportional to the excitation intensity of corresponding mode. Among the sub-reflection-valleys splitting from mode I, the valley with maximum depth should appear at the center just as displayed in Fig. 5.

Next, we focus on mode VI. As a TM-polarized mode, the direction of field is just opposite to the TE-polarized mode, i.e., the magnetic field is perpendicular to the plane determined by z axis and $\overline{\beta}_{VI}$. Base on the same infer-

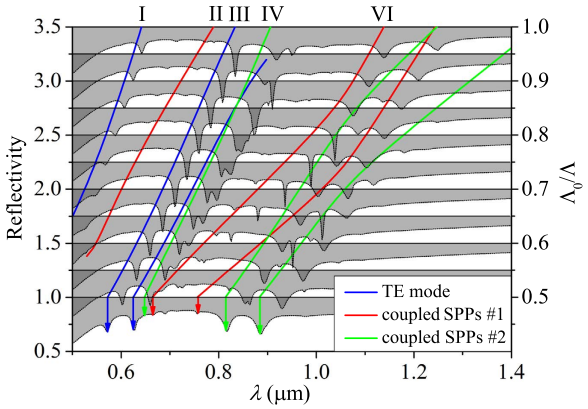

Figure 6. The reflection spectra of normal incidence changing with the QC constant Λ ($\Lambda_0 = 1\,\mu m$). The blue, red, and green lines are the dispersion relation from the mode analysis (dispersion relation $\beta(\lambda)$ with equation (18)). The vertical axis corresponds to $\Lambda = 2\,\mu m(\Lambda_0/\Lambda = 0.5)$. Others shift up $\Delta R = 0.25$ for the spectra by tune, corresponding to $\Delta(\Lambda_0/\Lambda) = 0.5$ as right labels shown.

ence, the splitting modes with $\overline{\beta}_{VI}$ close to the y axis should have the consistent field direction with the incidence and should be strongly excited. Hence, the deepest valley should appear at two sides as shown in Fig. 5.

It is noteworthy that the SPPs of mode II, IV and VI in Fig. 3(a) are excited with the different intensities. That is, mode II is weakly excited, while mode IV and VI are strong. To understand this difference, we plot the reflectivity spectra changing with the QC constant Λ in Fig. 6. According to equation (17) and mode analysis, each value of $|\overline{k}_m|$ corresponds to three surface modes (seen as a group). There are three main values of $|\overline{k}_m|$ for the condition of $d = 0.4\Lambda$. Therefore, nine dispersion relations in three group should be found as the color solid lines in Fig. 6:

$$|\vec{\beta}(\lambda)| = |\vec{k}_m(\Lambda)| = |\vec{k}_{m,0}|(\Lambda_0/\Lambda) \tag{18}$$

$\overline{k}_{m,0}$ is the reciprocal vector when $\Lambda_0 = 1\,\mu m$ and the three main $|\vec{k}_{m,0}|$'s in Fig. 3(c) are $2\pi\sec(\pi/10)\,\mu m^{-1}$, $8\pi\sin(\pi/10)\,\mu m^{-1}$ and $4\pi\,\mu m^{-1}$, corresponding to the radiuses of three circles. The blue lines are the dispersion relations of the TE mode. The strong coupling between SPPs on the upper and lower metal surface leads to the break off of the SPPs dispersion relations. The former part of the green lines together with the latter part of the red lines are the SPPs dispersion relations along the upper metal surface, and the former part of the red lines together with the latter part of the green lines are the SPPs dispersion relations along the lower metal surface. By comparing dispersion relations with the reflection spectra, TE modes would be always strongly excited until the cut-off wavelength $\lambda \sim 0.9\,\mu m$, when the thickness of quasicrystalline layer is too thin to afford TE mode. It also found that the SPPs on the upper metal surface are easy to be excited, while the SPPs on the lower metal surface are difficult to. Similar phenomenon could also be found in the asymmetric metal/dielectric corrugated structures[28]. The coupling process doesn't exist between groups because of the magnitude of $|\vec{k}_m|$ being different. Back to the spectrum in Fig. 3(a), mode II at $\lambda = 0.789\,\mu m$ is the SPPs on the lower metal surface, which is difficult to be excited. The other two mode, IV and VI, belong to the SPPs on the upper metal surface, which could be strongly excited.

Summary

We have numerically studied the broadband multiple responses of the surface modes in 2D photonic QC/metal structures. The 2D photonic QC here refers to the the dielectric cylinders patterned in Penrose tiling. We also improve the RCWA method so that it can handle quasicrystalline lattice. When the cut-off percentage of reciprocal vectors is chosen to be 5% (i.e., 231 reciprocal vectors are chosen to be the base vectors), the calculation shows an accurate enough results with acceptable efficiency.

Six main responses on the normal incidence spectrum, which correspond to three SPPs modes and three TE modes, are observed. Each mode multiply splits to 2∼4 sub-modes at oblique incidence. If the incident wave is TM-polarized, the sub-modes have the maximum response on the center for TE mode and on two sides for SPPs. If we change the polarization of incidence, the position of the maximum response would change too.

The excitation frequency of the proposed structure is determined by the phase matching condition. However, not all of the excitation frequencies satisfying phase matching condition can be found on the reflection spectrum and the excitation intensities of some modes are too weak to be observed on the spectrum. On one hand, the SPPs on the lower metal surface is unable to be excited strongly. The main indication of its existence is the break-off of the dispersion relations of the SPPs on the upper surface, which is caused by the coupling between the two SPPs modes. The coupling between other modes are not found. On the other hand, the excitation intensity also depends on the angle between incident field and mode field. It means that some sub-modes at oblique incidence might be too weak to present on the spectrum.

References

1. Bauer, C., Kobiela, G. & Giessen, H. 2d quasiperiodic plasmonic crystals. *Sci. Rep*. **2** (2012).
2. Bauer, C. & Giessen, H. Light harvesting enhancement in solar cells with quasicrystalline plasmonic structures. *Opt. Express* **21,** A363–A371 (2013).
3. Gong, Y., Liu, X., Wang, L., Lu, H. & Wang, G. Multiple responses of tpp-assisted near-perfect absorption in metal/fibonacci quasiperiodic photonic crystal. *Opt. Express* **19,** 9759–9769 (2011).
4. Xue, J. *et al.* Surface plasmon enhanced transmission through gold planar crystals with various aperture arrangements. *Microelectronic Engineering* **87,** 1340–1343 (2010).
5. Suck, J.-B., Schreiber, M. & Häussler, P. *Quasicrystals: An introduction to structure, physical properties and applications* vol. 55 (Springer Science & Business Media, 2013).
6. Verre, R. *et al.* Quasi-isotropic surface plasmon polariton generation through near-field coupling to a penrose pattern of silver nanoparticles. *ACS nano* **8,** 9286–9294 (2014).
7. Cui, Y. *et al.* Ultrabroadband light absorption by a sawtooth anisotropic metamaterial slab. *Nano Lett*. **12,** 1443–1447 (2012).
8. Sun, L., Cheng, H., Zhou, Y. & Wang, J. Broadband metamaterial absorber based on coupling resistive frequency selective surface. *Opt. Express* **20,** 4675–4680 (2012).
9. Vardeny, Z. V., Nahata, A. & Agrawal, A. Optics of photonic quasicrystals. *Nat. Photonics* **7,** 177–187 (2013).
10. Kasture, S. *et al.* Plasmonic quasicrystals with broadband transmission enhancement. *Scientific reports* **4** (2014).
11. Ravishankar, A. P., Yallapragada, V., Kasture, S., Nagarajan, A. & Achanta, V. G. Broadband linear and nonlinear optical response of plasmonic quasicrystals. *Optics Communications* **366,** 57–60 (2016).
12. Nguyen, T. D., Nahata, A. & Vardeny, Z. V. Measurement of surface plasmon correlation length differences using fibonacci deterministic hole arrays. *Opt. Express* **20,** 15222–15231 (2012).
13. Achanta, V. G. Plasmonic quasicrystals. *Progress in Quantum Electronics* **39,** 1–23 (2015).
14. Deng, Z.-L., Li, Z.-H., Dong, J.-W. & Wang, H.-Z. In-plane plasmonic modes in a quasicrystalline array of metal nanoparticles. *Plasmonics* **6,** 507–514 (2011).
15. Dallapiccola, R., Gopinath, A., Stellacci, F. & Dal Negro, L. Quasi-periodic distribution of plasmon modes in two-dimensional fibonacci arrays of metal nanoparticles. *Optics express* **16,** 5544–5555 (2008).
16. Forestiere, C., Miano, G., Rubinacci, G. & Dal Negro, L. Role of aperiodic order in the spectral, localization, and scaling properties of plasmon modes for the design of nanoparticle arrays. *Physical Review B* **79,** 085404 (2009).
17. Gopinath, A., Boriskina, S. V., Feng, N.-N., Reinhard, B. M. & Negro, L. D. Photonic-plasmonic scattering resonances in deterministic aperiodic structures. *Nano letters* **8,** 2423–2431 (2008).
18. Chan, Y., Chan, C. & Liu, Z. Photonic band gaps in two dimensional photonic quasicrystals. *Phys. Rev. Lett*. **80,** 956 (1998).
19. Namin, F. A. & Werner, D. H. Rigorous analysis of diffraction from quasicrystalline gratings via floquet¡¯s theorem in higher-dimensional space. *ACS Photonics* **1,** 212–220 (2014).
20. Moharam, M., Gaylord, T., Grann, E. B. & Pommet, D. A. Formulation for stable and efficient implementation of the rigorous coupled-wave analysis of binary gratings. *JOSA A* **12,** 1068–1076 (1995).
21. Ho, I.-L., Lee, M.-T. & Chang, Y.-C. Coupled-wave theory for birefringent photonic quasicrystal structures. *J. Opt. Soc. Am. B* **29,** 382–388 (2012).
22. Chang, Y.-C. & Xie, H.-Y. Effecient computation methods for 3d microscopic ellipsometry. In *International Workshop on Computational Science and Engineering* (*IWCSE 2013*) (2013).
23. Levine, D. & Steinhardt, P. J. Quasicrystals. i. definition and structure. *Phys. Rev. B* **34,** 596 (1986).
24. Levine, D. & Steinhardt, P. J. Quasicrystals: a new class of ordered structures. *Phys. Rev. Lett*. **53,** 2477 (1984).
25. De Bruijn, N. Algebraic theory of penrose's non-periodic tilings of the plane. i. In *Indagationes Mathematicae* (*Proceedings*) vol. 84, 39–52 (Elsevier, 1981).
26. Moharam, M., Gaylord, T., Pommet, D. A. & Grann, E. B. Stable implementation of the rigorous coupled-wave analysis for surface-relief gratings: enhanced transmittance matrix approach. *JOSA A* **12,** 1077–1086 (1995).
27. Rakic′, A. D., Djurišic′, A. B., Elazar, J. M. & Majewski, M. L. Optical properties of metallic films for vertical-cavity optoelectronic devices. *Appl. Optics* **37,** 5271–5283 (1998).
28. Hooper, I. R. & Sambles, J. R. Surface plasmon polaritons on thin-slab metal gratings. *Phys. Rev. B* **67,** 235404 (2003).

Acknowledgements

This work is supported by the National Key Basic Research Program of China (2013CB328702) and the National Natural Science Foundation of China(11374074, 11176009).

Author Contributions

H.Y. and F.H. derived the algorithm. H.Y. and X.J. wrote and run the programs. H.Y. and X.S. analysed the results. All authors reviewed the manuscript.

Additional Information

Competing financial interests: The authors declare no competing financial interests.

How to cite this article: Yuan, H. *et al.* Broadband multiple responses of surface modes in quasicrystalline plasmonic structure. *Sci. Rep.* **6**, 30818; doi: 10.1038/srep30818 (2016).